Journal of Power Sources 673 (2026) 239725

Contents lists available at ScienceDirect

Journal of Power Sources

journal homepage: www.elsevier.com/locate/jpowsour

Impedance-based analysis of PEMFC degradation phenomena during accelerated stress tests

Sebastian Raab *, André Weber

Institute for Applied Materials – Electrochemical Technologies (IAM-ET), Karlsruhe Institute of Technology (KIT), Adenauerring 20b, 76131, Karlsruhe, Germany

HIGHLIGHTS

- In-operando EIS with DRT separates kinetic, ionomer, and mass transport losses.
- TLM quantifies charge transfer, ionomer and mass transport resistances during ASTs.
- Low-potential cycling primarily raises kinetic losses consistent with ECSA loss.
- High-potential cycling raises kinetic/transport losses due to structural degradation.
- Ex-situ diagnostics validate impedance-derived resistance evolution and mechanisms.

ARTICLE INFO

Keywords:
Polymer electrolyte membrane fuel cell
Durability
Accelerated stress test
Electrochemical impedance spectroscopy
Distribution of relaxation times
Transmission line model
Cathode catalyst layer

ABSTRACT

Degradation of the cathode catalyst layer (CCL) limits the durability of polymer electrolyte membrane fuel cells (PEMFCs) by reducing the electrochemically active surface area and impairing oxygen transport. These co-occurring effects are difficult to disentangle with standard electrochemical diagnostics. In this study, we used impedance-based analysis to quantify the individual contributions of catalyst and carbon support degradation in PEMFCs subjected to accelerated stress tests (ASTs): low-potential cycling (0.6–0.95 V, 55 000 cycles) and high-potential cycling (1.0–1.5 V, 50 000 cycles).

In-operando electrochemical impedance spectroscopy under H_2/air and impedance data analysis using the distribution of relaxation times and transmission line modeling were combined with complementary diagnostic techniques. This approach separated the ohmic, charge transfer, CCL ionomer, and mass transport resistances and tracked their evolution during ASTs.

Low-potential cycling increased the charge transfer resistance by 29–56%, consistent with a loss of active surface area. High-potential cycling resulted in increased charge transfer, mass transport, and ohmic resistances, with a 77% reduction in CCL thickness, indicating severe carbon corrosion and collapse of the CCL structure. The resulting framework provides a practical tool to screen cathode materials and operating strategies by quantitatively linking specific degradation modes to electrochemical loss processes.

1. Introduction

Polymer electrolyte membrane fuel cells (PEMFCs) can have a significant impact on the future of sustainable energy conversion. Due to their low operating temperatures, short start-up times, and high gravimetric and volumetric energy densities, PEMFCs can play a key role in decarbonizing the mobility sector, especially for heavy-duty applications [1]. For the future success of the PEMFC technology, further improvements in performance, cost, and durability are crucial [2].

Over the past few decades, advances in PEMFCs have significantly improved performance and lifetime [2]. Today, standard PEMFC catalyst layers are composed of a carbon support structure with finely dispersed platinum (Pt) catalyst particles and an ionomer film. The catalyst layers can account for 30–40% of voltage degradation during urban driving cycles [3] and for half the costs of automotive PEMFC systems [4]. The platinum-group metal (PGM) catalyst is central to PEMFC performance, durability, and cost [5]. To maximize PGM utilization, these metals are finely dispersed on the carbon support structure. However, such fine dispersion can accelerate degradation during operation [6–9], ultimately reducing PEMFC durability.

* Corresponding author.
E-mail address: sebastian.raab@kit.edu (S. Raab).

https://doi.org/10.1016/j.jpowsour.2026.239725
Received 19 December 2025; Received in revised form 8 February 2026; Accepted 22 February 2026
Available online 27 February 2026

Accelerated stress tests (ASTs) are widely used to analyze and quantify PEMFC degradation [10]. These protocols reduce testing time and costs and are specifically designed to degrade certain components of PEMFCs (membranes, electrodes, etc.) or to mimic specific operating conditions, such as start-up/shut-down (SU/SD) operation or driving cycles [11]. The AST protocols published by the U.S. Department of Energy (DOE) [11] have been widely used and include protocols to specifically degrade the PEMFC catalyst by square-wave low-potential cycling (0.6–0.95 V) and the carbon support structure by triangular-wave high-potential cycling (1.0–1.5 V). All protocols are conducted under H_2/N_2 (anode/cathode) conditions.

Numerous studies have used potential cycling AST protocols under H_2/N_2 conditions to assess cathode catalyst layer (CCL) degradation. **Low-potential cycling ASTs** have been applied to analyze catalyst degradation in CCLs, considering various catalyst materials and compositions [12], platinum loadings [13], and layer thicknesses [14]. Other studies investigated how low-potential cycling affects different carbon supports (Vulcan/Ketjenblack) [15], the relationship between H_2/air performance and roughness factor [16], and the effects of cathode gases (air/N_2) and humidity [17]. Stariha et al. [10] explored the effect of high- and low-potential cycling, as well as high-potential holding, on different carbon support types (Pt/HSAC, Pt/V, Pt/LSAC). They found much stronger degradation under square-wave cycling than under triangular-wave cycling in similar voltage ranges (0.6–1.0 V).

High-potential cycling ASTs, emulating critical SU/SD operations, have been applied to examine the effect of various catalysts and catalyst layer compositions on carbon corrosion [18], the evolution of cathode catalyst interfaces [19], and the effect of the CCL ionomer-to-carbon (I/C) weight ratio on carbon corrosion [20,21]. Among others, they have also been deployed to examine the in- and through-plane non-uniformity of carbon corrosion [22] and the corrosion of carbon nanofibers [23].

Electrochemical impedance spectroscopy (EIS) is a well-established technique for analyzing PEMFC degradation. EIS under H_2/air (anode/cathode) conditions is a non-invasive, in-operando analysis technique that captures all faradaic processes and the effect of intrinsic humidification. However, the separation and quantification of the various electrochemical loss processes can be challenging due to overlapping in the characteristic frequency range and reciprocal interferences [24].

A powerful method for analyzing impedance data is the **distribution of relaxation times (DRT)**, which enables the precise identification and separation of various electrochemical processes based on their characteristic relaxation times and their dependence on operating conditions, without prior knowledge of the processes [25–29]. The DRT has been applied in multiple publications to analyze the degradation of PEMFC stacks and to identify defective cells [30–36]. Other publications have deployed DRT to analyze degradation in single PEMFCs, focusing on carbon corrosion during low-potential cycling [37], the effect of the I/C weight ratio in the CCL on carbon corrosion behavior [20,21], the influence of cathode gas recirculation on PEMFC durability [38], and the effect of high-potential holding [37,39]. Others have used the DRT to analyze degradation during idling conditions [40], degradation of high-oxygen-permeability ionomers (HOPIs) during catalyst ASTs [41], and the impact of microporous layers (MPLs) on gas diffusion layer (GDL) degradation [42].

Some studies used the DRT to analyze carbon corrosion behavior via high-potential holding tests [37,39]. Because the carbon corrosion rate increases exponentially with the cathode potential [43], holding tests at fixed potentials are difficult to compare and do not capture the dynamic SU/SD potential swings up to 1.6 V [44,45]. The DOE high-potential cycling AST (1.0–1.5 V), which typically induces much higher corrosion rates than high-potential holding [10,11], was therefore chosen in this study to emulate the dynamic SU/SD conditions.

The resolution of AST-induced catalyst and carbon degradation in CCLs is achieved through combined impedance data analysis using DRT and a transmission line model (TLM). This enables a comprehensive in-situ and in-operando assessment of the effects of the degradation mechanism on electrochemical processes. DRT enables the deconvolution of characteristic relaxation frequencies of impedance spectra. However, peak fitting is ambiguous when processes overlap or when a complex coupling between transport and charge transfer processes results in TLM behavior. Here, DRT is applied to establish a physicochemically meaningful TLM and to provide initial values for complex nonlinear least squares (CNLS) fitting. This approach enables quantification of ohmic, charge transfer, ionomer, and mass transport resistances under different operating conditions and aging states. The obtained results are compared with complementary ex-operando diagnostics (CV, EIS under H_2/N_2, and limiting current measurements). Such combined diagnostics strengthen the interpretation of the underlying degradation mechanisms and support the distinction between catalyst- and carbon-support-related degradation pathways. To the best of the authors' knowledge, DRT and subsequent TLM fitting have not been applied to analyze the effect of carbon-corrosion-induced degradation from high-potential cycling under the DOE protocol [11]. Analysis of impedance spectra measured during standardized DOE low- and high-potential AST protocols provides a controlled basis for distinguishing catalyst-related degradation from carbon-support-driven structural degradation.

In this study, we exposed commercial 1 cm^2 PEMFCs to low- and high-potential cycling ASTs [11] and applied EIS, DRT, and subsequent transmission line modeling, complemented by cyclic voltammetry (CV), EIS (H_2/N_2), limiting current measurements, and cross-sectional analysis, to separate catalyst- and carbon-corrosion-related loss processes. A detailed three-dimensional analysis of microstructural changes within the catalyst layers (e.g., by tomography or electron microscopy) is beyond the scope of this study. Instead, we inferred microstructural evolution indirectly from the combined evolution of the electrochemical resistances (R_{ct}, R_{ion}, R_{mt}, R_0), the distribution of relaxation times, and the cross-sectional thicknesses of the MEA layers. The combination of in-situ and ex-situ techniques for analyzing degradation behavior provides a holistic picture of how catalyst and carbon corrosion affect electrochemical loss processes under real-life operating conditions.

2. Experimental and modeling

Testing setup. – Differential single PEMFCs with an active cell area of 1 cm^2 were operated at high gas stoichiometries and a constant volumetric flow rate. This setup ensured a gradient-free environment in the gas channels. At 2 A cm^{-2}, the minimum gas stoichiometry was 9.7 for the anode and 6.1 for the cathode. Anode and cathode humidification were provided independently via combustion humidification in two catalytic burner chambers [24]. During operation, synthetic air (O_2/N_2) was fed to the cathode at a total pressure of 1.0 bar. The dry oxygen partial pressure was adjusted to 0.315 atm, which corresponds to ambient air at 1.5 bar absolute. Four combined humidity/temperature sensors, SHT41 (Sensirion, Staefa, Switzerland), were placed upstream and downstream of the cell housing to monitor inlet and outlet conditions. Electrochemical measurements were performed with a Zennium E potentiostat (Zahner, Kronach, Germany) in a four-point configuration. The test bench and cell housing, developed in-house [24,46], enabled precise control of the active cell area contacting pressure, which was set to 0.5 MPa in all experiments. Both the anode and cathode flow fields consisted of a parallel channel/rib design (rib width, channel width, and depth: 1 mm). The flow fields were manufactured from gold to minimize contact resistance. Commercial, state-of-the-art MEAs were used, with estimated catalyst loadings of 0.41 mg_{Pt} cm^{-2} (cathode) and 0.07 mg_{Pt} cm^{-2} (anode). The gas diffusion layer H14CX483 (Freudenberg, Weinheim, Germany) was used for both electrodes [47].

Testing procedures. – A detailed description of all applied electrochemical characterization techniques is provided in Table S1. The **break-in procedure** consisted of multiple potential holds and cycles

between open-circuit voltage (OCV) and various potentials down to 0.6 V at 80 °C. The break-in procedure was performed at 95% and 32% relative humidity (RH), each applied symmetrically (anode/cathode), as described in Ref. [48].

Electrochemical characterizations were performed immediately following the break-in procedure to ensure sample stability. The complete electrochemical characterization sequence was repeated at AST cycle intervals ranging from 10 to 5 000 cycles. Prior to each characterization, a **voltage recovery procedure** was performed at 40 °C and 80% RH**.** The characterization protocol included polarization curves (80 °C, 70% RH), EIS under H_2/air and H_2/N_2 conditions (both at 80 °C, 70% RH), cyclic voltammetry of the cathode (50 °C, 95% RH), and limiting current measurements (80 °C, 70% RH) with nitrogen and helium as inert gas on the cathode side.

Polarization curves were recorded galvanostatically with a Keysight DC Power Supply E3644A and a Keysight Data Acquisition/Switch Unit 34970A (Keysight, Santa Rosa, USA). The current density was ramped up to the maximum value defined by a cut-off cell voltage of 0.3 V, then ramped down [49]. Unless noted otherwise, only the down-sweep (decreasing current density) polarization curves are reported below.

EIS under H_2/air conditions was recorded with a Zahner Zennium E potentiostat. All spectra (H_2/air) were recorded galvanostatically at several current densities (0.25–1.4 A cm^{-2}) in the frequency range of 0.5 Hz to 1 MHz and with a perturbation amplitude of 1–10 mA. **EIS under H_2/N_2** conditions was recorded potentiostatically at 0.5 V in the frequency range of 0.5 Hz to 1 MHz, with a perturbation amplitude of 20 mV.

Cyclic voltammetry [50] was performed to determine the roughness factor (RF) of the CCL, the double-layer capacitance (DLC), and the hydrogen crossover current density. Each CV was performed between 0.05 V and 1.2 V for 10 cycles, at slew rates of 150 and 400 mV s^{-1}. Unless otherwise stated, only the data from the final cycle at 150 mV s^{-1} were analyzed and shown in the figures. Prior to the measurements, the cathode was purged with nitrogen for 5 min, then the cathode nitrogen flow was stopped. The **roughness factor** was calculated using the standard HAD (hydrogen adsorption and desorption) method by integrating the hydrogen adsorption area (0.05 V to 0.4–0.5 V) and referencing it to the geometrical MEA area (1 cm^2). The **DLC** was determined from the difference in current density between potential sweeps at 150 and 400 mV s^{-1} in the 0.4–0.5 V range [51]. The area-specific DLC (mF cm^{-2}) was then calculated by normalizing the slope of current density difference versus scan rate by the geometric cell area (1 cm^2).

Limiting current measurements were performed to evaluate molecular diffusion resistance and the combined Knudsen and film diffusion resistance. Measurements covered cathode oxygen concentrations of 1%, 2%, 3%, 4%, and 5% in nitrogen and in helium as the inert gases. A detailed description of the approach is provided in the supplementary material [52,53].

The **electrochemical characterization** combined in-operando methods (polarization curves, EIS with H_2/air, limiting current measurements) and ex-operando methods (EIS with H_2/N_2, CV). In H_2/air operation, product water improves membrane hydration but can hinder gas access, while ex-operando tests lack water generation and thus operate at lower internal hydration. Table S2 provides an overview of all techniques, including their characteristics and limitations.

Accelerated stress tests. – The ASTs followed U.S. DOE protocols [11] with two approaches: square-wave low-potential cycling (0.6–0.95 V, 16 s dwell time) and triangular-wave high-potential cycling (1.0–1.5 V, 3 s cycle time), both under H_2/N_2 conditions at 80 °C and 95% RH. To accelerate catalyst degradation, 55 000 low-potential cycles (LPCs) were used. To emulate SU/SD-induced carbon corrosion, 50 000 high-potential cycles (HPCs) were applied.

MEA layer thicknesses were determined via **cross-sectional analysis** with a VHX-7000 digital microscope (Keyence, Osaka, Japan).

Impedance data analysis. – The impedance spectra were validated by Kramers-Kronig validity tests [54], where all spectra showed residual errors below 1%. To separate the electrochemical processes by their characteristic relaxation times [55,56], we analyzed the spectra using DRT with the Tikhonov regularization ($\lambda = 0.001$, 20 time constants per decade). The regularization parameter (λ) was adopted in accordance with Heinzmann et al. [24], who showed it provided stable peak separation for PEMFC spectra in a comparable frequency range. The regularization parameter was kept constant across all datasets to ensure consistent trend analysis during aging. The allocation of the DRT peaks to specific loss processes was achieved by systematically varying the operating conditions, as introduced by Heinzmann et al. [25].

The CCL was modeled using a transmission line model that couples the electronic and ionic paths via charge transfer at the triple-phase boundary (TPB) [25,46]. In series, the membrane resistance was modeled as an ohmic resistance (R_0), and the mass transport resistance (CCL, GDL, and MPL) as a generalized finite-length Warburg element (GFLW) [57]. The ohmic resistances were corrected by 0.014 Ω cm^2 to remove the setup contributions, determined from ex-operando measurements. Overall, the TLM impedance of a porous CCL (Z_{TLM}) can be described as follows [25,58]:

$$Z_{TLM}^{H_2/air}(\omega) = \frac{\chi_{ion}\chi_{el}}{\chi_{ion}+\chi_{el}} \cdot \left(L + \frac{2\kappa(\omega)}{\sinh\left(\frac{L}{\kappa(\omega)}\right)} \right) + \kappa(\omega) \cdot \frac{\chi_{ion}^{\,2}+\chi_{el}^{\,2}}{\chi_{ion}+\chi_{el}} \cdot \coth\left(\frac{L}{\kappa(\omega)}\right) \quad [1]$$

This TLM expression accounts for the length-specific resistances of the ionic (χ_{ion}, Ω m^{-1}) and electronic (χ_{el}, Ω m^{-1}) paths. An overview of all relevant TLM parameters, their descriptions, and units is provided in Table S3. $\kappa(\omega)$ is the frequency-dependent characteristic length (penetration depth of $\chi_{ion} \gg \chi_{el}$) of the TLM, set by the ratio of charge transfer impedance (ξ, Ω m) to the sum of length-specific resistances in the TLM (χ_{ion} and χ_{el}).

$$\kappa(\omega) = \sqrt{\frac{\xi(\omega)}{\chi_{ion}+\chi_{el}}} \quad [2]$$

The charge transfer impedance is modeled by an RQ element, accounting for the thickness-specific charge transfer resistance (r_{ct}, Ω m) and the characteristic relaxation time of the charge transfer (τ_{ct}, s) [25].

$$\xi(\omega) = \frac{r_{ct}}{1+(i\,\omega\,\tau_{ct})^n} \quad [3]$$

Regarding the CCL thickness (L), the beginning-of-life (BoL) value of 15.8 µm was determined by optical microscopy. CCL thickness was measured only at BoL and end of life (EoL), while its evolution during cycling is unknown. Therefore, L was kept constant at the BoL value for all equivalent circuit model (ECM) fits. As a result, thickness-dependent parameters are interpreted as effective values referenced to the BoL geometry. Area-specific charge transfer and ionomer resistance are calculated using the BoL thickness (Eqs. (5) and (6)) for consistent comparison across all aging stages. Table S4 shows that, after converting to area-specific values, charge transfer and ionomer resistance calculated for BoL (15.8 µm) and EoL (3.7 µm) thicknesses are identical within the fitting uncertainty. Parametric variations of the CCL electronic resistance (χ_{el}) in the TLM (see Table S5 and Fig. S1) showed that only substantial increases in χ_{el} (>100 Ω m^{-1}) produced a noticeable rise in the high-frequency intercept. These changes are several orders of magnitude larger than the typical CCL electronic resistances reported in the literature (1.65 to 83.3 mΩ m^{-1}) [59,60]. A pronounced increase in electronic resistance could occur in severely corroded CCLs if carbon corrosion collapses the support structure and disconnects parts of the carbon network. However, other mechanisms could also raise the high-frequency intercept, such as CCL delamination or increased contact resistances. Furthermore, the 77% reduction in CCL thickness (Table S8)

shortens the geometric through-plane path length. Thus, attributing the entire rise of the high-frequency intercept to a distributed electronic limitation would require an extreme drop in effective CCL conductivity. This effect cannot be distinguished from interfacial or contact contributions based solely on impedance data. For these reasons, we set the CCL electronic resistance to zero in the TLM ($\chi_{el} \approx 0$) and attributed the observed increase in the high-frequency intercept to a collective ohmic contribution, including membrane, contact, and interface resistances, rather than a uniquely identifiable distributed electronic resistance within the corroded CCL. Assuming negligible electronic resistance in the CCL ($\chi_{el} \approx 0$), this simplifies the complex TLM in Eq. (1):

$$Z_{TLM}^{H_2/air}(\omega) = \kappa(\omega) \cdot \chi_{ion} \cdot coth\left(\frac{L}{\kappa(\omega)}\right) \quad [4]$$

In the DC limit ($\omega \rightarrow 0$), the expression becomes purely real and can be interpreted as the charge transfer resistance in series with the CCL ionomer resistance. This approximation is applicable only to well-designed PEMFC electrodes, where the penetration depth is comparable to the electrode thickness, ensuring that the applied catalyst is effectively utilized [46]. Symmetrical cell tests (H_2/H_2 conditions) showed negligible polarization resistance of the hydrogen oxidation reaction (HOR) and mass transport within the anode (<0.0118 Ω cm^2) under the applied testing conditions (Fig. S2). This anode resistance accounts for less than 6% of the cell's overall polarization resistance, in good agreement with our previous study [24]. The anode's contribution to the total resistance was therefore neglected in the further analysis. Ohmic resistance, mass transport resistance, charge transfer resistance, and ionomer resistance in the CCL were determined by fitting the ECM to the EIS and DRT data using CNLS fitting [61]. The overall area-specific charge transfer resistance (R_{ct}, Ω cm^2) of the cathode, considering the thickness-specific charge transfer resistance (r_{ct}, Ω m), the CCL thickness at the BoL (L), and the active cell area (A) of 1 cm^2, was calculated using Eq. (5).

$$R_{ct} = \frac{r_{ct} \cdot A}{L} \quad [5]$$

The effective area-specific ionomer resistance (R_{ion}^{eff}, Ω cm^2) in the CCL can be calculated using the length-specific ionomer resistance (χ_{ion}, Ω m^{-1}) of the TLM by Eq. (6).

$$R_{ion}^{eff} = \frac{1}{3} \cdot \chi_{ion} \cdot L \cdot A \quad [6]$$

The local ionic current density is not constant throughout the entire CCL thickness, decreasing from the membrane towards the catalyst layer surface [46]. To account for this non-uniformity, a factor of 1/3 [62,63] is considered in Eq. (6).

In this study, all ionomer resistances in the CCL were calculated using Eq. (6). To improve readability, this value is hereafter referred to as CCL ionomer resistance (R_{ion}) throughout this publication. The effective area-specific capacitance (C_{ct}, F cm^{-2}) was calculated from the characteristic frequency of the charge transfer resistance (f_{ct}, Hz) and the charge transfer resistance (R_{ct}) [64,65]:

$$C_{ct} = \frac{1}{2 \cdot \pi \cdot f_{ct} \cdot R_{ct}} \quad [7]$$

For EIS under H_2/N_2 conditions, the cathode was treated as blocking (without Faradaic charge transfer). Accordingly, the charge transfer impedance (Eq. (3)) was simplified to represent only the double-layer response by replacing it with a pure constant phase element (CPE). Subsequently, this term was inserted into Eq. (2) and the simplified TLM expression (Eq. (4)). This substitution leads directly to the expression in Eq. (8) [62]. An ECM consisting of a series of an ohmic resistance, an inductive element, and the TLM described in Eq. (8) was used to fit the H_2/N_2 impedance spectra. Here, Q and n denote the CPE coefficient and exponent, respectively.

$$Z_{TLM}^{H_2/N_2}(\omega) = \sqrt{\frac{\chi_{ion}}{Q \cdot (j \cdot \omega)^n}} \cdot coth\left(L \cdot \sqrt{\chi_{ion} \cdot Q \cdot (j \cdot \omega)^n}\right) \quad [8]$$

3. Results and discussion

3.1. Polarization curves and cyclic voltammetry

During **low-potential cycling**, the polarization curves (Fig. 1a) and the areas under the hydrogen desorption/adsorption peaks of the CV curves (Fig. 1c) exhibit a steady decrease. This decrease is attributed to the dissolution and agglomeration of catalyst particles, which reduces the electrochemically active surface area (ECSA) [66]. During **high-potential cycling**, two phases with varying severities of degradation can be identified. In the first phase, up to 10 000 HPCs, the polarization curves (Fig. 1b) show only a slight decrease. A drastic decline follows in the second phase. This evolution can be attributed to the collapse of the carbon support structure due to continuous carbon corrosion at high potentials [22,67–69]. This leads to a significant increase in internal losses, resistances, and overvoltages, ultimately resulting in decreased performance. Severe microstructural changes in the CCL, such as a reduction in carbon support structure pore size, have been reported during high-potential cycling between 1.0 V and 1.5 V [22] and during high-potential holding at 1.4 V [37]. The decrease in hydrogen desorption and adsorption peaks in the CV curves with HPCs (Fig. 1d) is due to ongoing carbon support loss. Additionally, CCL thinning removes catalyst particles located on the corroded carbon particles [19]. Although carbon support ASTs are designed primarily to accelerate carbon corrosion and thus minimize catalyst degradation, Pt particle growth can still occur. High potentials and corrosion-induced loss of anchoring sites can promote Pt detachment, dissolution/redeposition, and coalescence, leading several studies to report increased particle size even under carbon corrosion protocols [70,71]. Neither the measured contacting force of the active cell area nor the cell temperatures changed significantly during low-potential (Table S6) and high-potential cycling (Table S7).

The polarization curve hysteresis between up- and down-sweeps decreases strongly during the first 10 000 LPCs (Fig. S3). This may result from degradation in water management and in the ability of the MEA, MPL, and GDL to retain produced liquid water [72].

3.2. Cell voltages and ohmic resistances at various current densities

During **low-potential cycling** (Fig. 2a), the cell voltages decrease steadily at all current densities. The voltage degradation rates range from 1.1 mV per 1 000 LPCs (0.2 A cm^{-2}) to 5.6 mV per 1 000 LPCs (1.8 A cm^{-2}). The ohmic resistance (R_0) in Fig. 2c remains relatively constant with the number of LPCs. This behavior indicates no significant membrane degradation or delamination of the catalyst layers. The integrity of the membrane was confirmed by the evolution of the OCV and the hydrogen crossover current density (Fig. S4a), which showed no long-term degradation during the LPCs.

In contrast, during **high-potential cycling** (Fig. 2b), the cell voltages remain relatively stable or even increase slightly until 5 000–10 000 cycles. After this point, the cell voltages decrease significantly at all current densities. Notably, the decrease is most pronounced at higher current densities, where mass transport losses in the GDL and CCL dominate. This trend may arise from severe microstructural changes, such as a collapse of the carbon structure, leading to a decrease in CCL porosity [67,69,70]. Consequently, oxygen transport to the TPB becomes increasingly impeded, resulting in a significant increase in mass transport losses. The ohmic resistance (Fig. 2d) remains relatively constant until 2 000 HPCs, but increases significantly afterward. The pronounced increase in ohmic resistance during high-potential cycling is not related to membrane degradation. Both the OCV and the hydrogen crossover current remain essentially constant over the entire AST

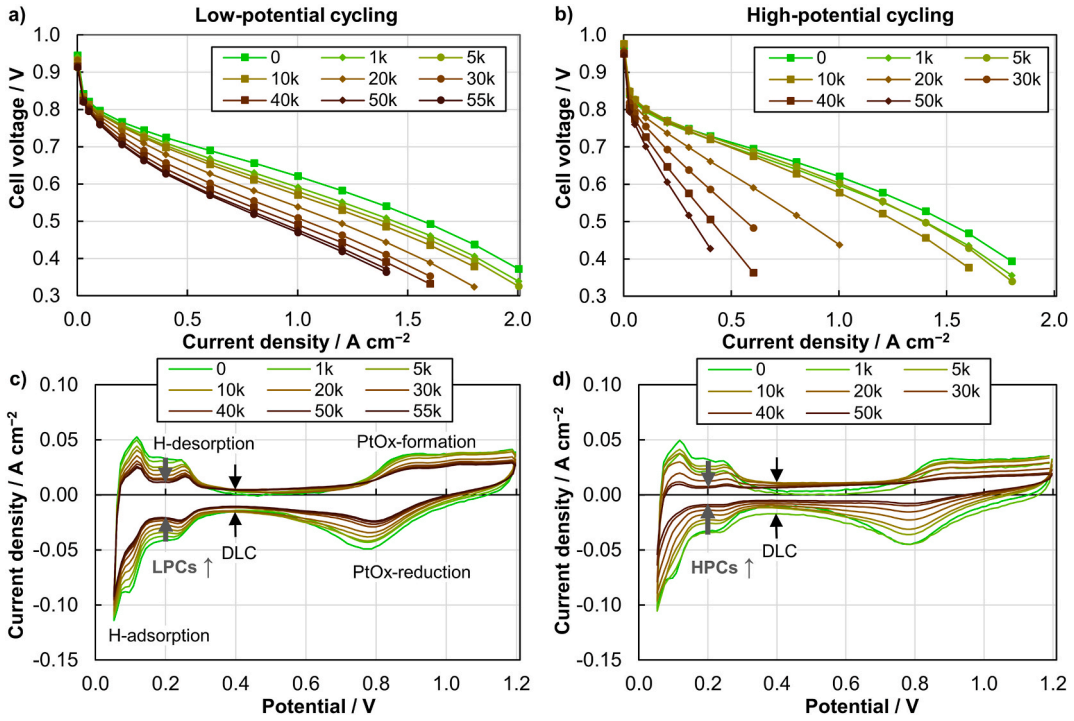

Fig. 1. Polarization curves (H_2/air, T = 80 °C, RH = 70% sym., $p_{O2,dry}$ = 0.315 atm, $\dot{V}$ = 200 sccm) and cyclic voltammograms of the cathode (H_2/N_2, 150 mV s^{-1}, T = 50 °C, RH = 95%, $\dot{V}$ = 200 sccm) during (a, c) 55 000 low-potential cycles (LPCs) and (b, d) 50 000 high-potential cycles (HPCs).

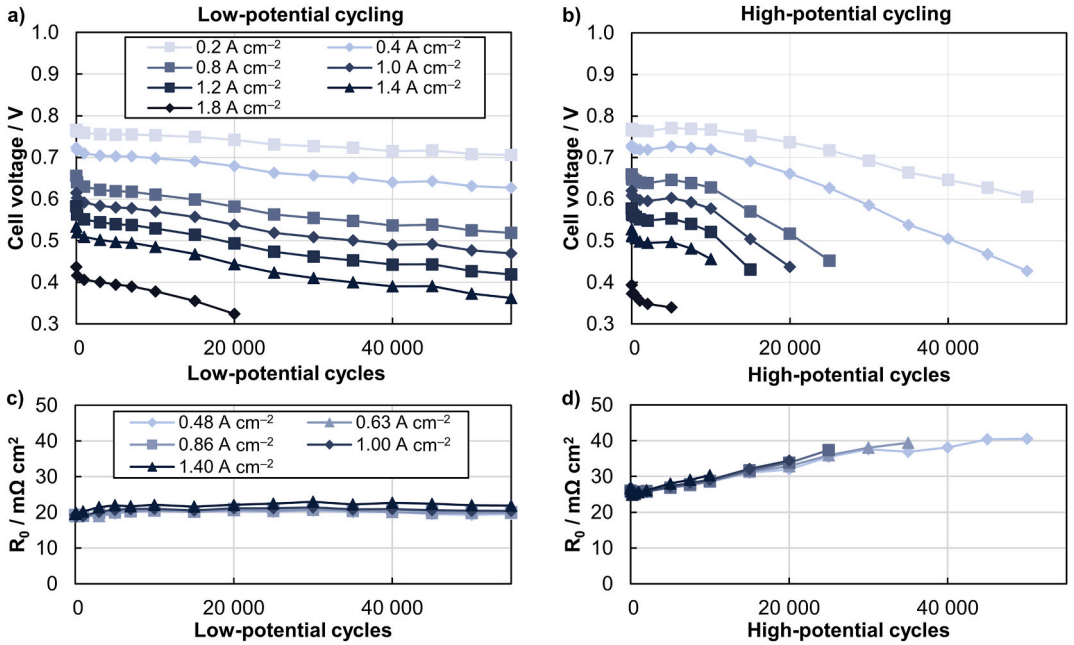

Fig. 2. Evolution of the cell voltage at 0.2–1.8 A cm^{-2} (H_2/air, T = 80 °C, RH = 70% sym., $p_{O2,dry}$ = 0.315 atm, $\dot{V}$ = 200 sccm) and ohmic resistance at 0.48–1.4 A cm^{-2} as a function of (a, c) low-potential cycles (LPCs) and (b, d) high-potential cycles (HPCs).

(Fig. S4), ruling out significant thinning or pinhole formation of the membrane. Instead, the observed behavior is consistent with carbon-corrosion-induced losses in electronic and interfacial conductivity, such as increased contact resistance at the CCL/MPL and CCL/membrane interfaces, or partial disconnection of the carbon network [71,73–75]. TLM simulations (Table S5 and Fig. S1) show that only very high electronic resistances of the CCL [59,60] can reproduce the experimentally observed increase in R_0, supporting the hypothesis of increased interfacial resistances.

3.3. Distribution of relaxation times at various current densities

EIS under H_2/air conditions was employed to determine the contributions of the various electrochemical loss processes to the performance degradation. Because the distribution of loss processes varies with current density, EIS measurements were recorded galvanostatically at

various current densities. The resulting Nyquist plots (Fig. S5), along with a magnified view of the high-frequency region (Fig. S6), are provided in the supplementary material. Notably, the polarization resistance increased significantly during both low-potential and high-potential cycling.

After collecting the EIS data, we used the **distribution of relaxation times** to separate mass transport (P1), oxygen reduction reaction (ORR) charge transfer (P2), and high-frequency peaks (P3–P5). The high-frequency peaks are commonly attributed to proton transport within the CCL ionomer phase [20]. They are also linked to subordinate anode processes [24], as supported by the DRT of EIS under H_2/H_2 conditions (Fig. S2b). The DRT analysis of EIS under H_2/air conditions supports process identification and enables tracking of the evolution of characteristic frequencies. It is important to note that quantitative resistance values reported in this work are extracted from ECM fitting of the impedance spectra rather than from integrating DRT peaks.

During **low-potential cycling**, the DRT (Fig. 3a, c, e) show a comparable evolution for all current densities: In the first 10 000 LPCs, the **mass transport resistance peak (P1)** decreases slightly (Figs. S7b, d, f), which suggests changes in the water management leading to the observed decrease in polarization curve hysteresis (Fig. S3a). The decrease in mass transport resistance is identified as the primary reason for the initial decrease in polarization resistance up to 10 000 LPCs. This initial decrease in mass transport resistance and polarization losses is consistent with reduced water retention.However, this interpretation is inferred from electrochemical trends and is not supported by direct measurements of liquid water content. It should therefore be regarded as a plausible explanation rather than definitive proof. After 10 000 LPCs, the mass transport peaks show no significant changes, indicating that oxygen transport in the GDL and CCL is not affected by the LPCs. The **ORR charge transfer resistance peak (P2)** remains relatively unchanged up to 10 000 LPCs. Afterward, it increases strongly, while its peak frequency at 0.48 A cm^{-2} shifts from 135 Hz (10 000 LPCs) to 192 Hz (55 000 LPCs). The increase in charge transfer resistance can be attributed to a reduction in the TPB area in the CCL due to catalyst particle dissolution and agglomeration. Kwon et al. [37] also reported a decrease in specific relaxation time of the charge transfer ($\tau_o = R_{ct} \cdot C_{dl}$) from 0.0077 s (129 Hz) to 0.0043 s (232 Hz) after 30 000 cycles (0.4–0.95 V) at 0.3 A cm^{-2}. They attributed the negative relaxation time shift to a deformation of pore depth and size in the CCL, resulting from a significant decrease in DLC but only minor changes in charge transfer resistance. In our case, a decrease in capacitance during LPCs (Fig. 5a) is also observed, suggesting possible structural changes in the CCL pore structure.

During **high-potential cycling,** the DRT (Fig. 3b, d, f) do not show significant changes until 5 000 HPCs. Afterward, the **mass transport resistance peak (P1)** increases strongly, indicating a deterioration of oxygen transport in the diffusive media, potentially due to a decrease in hydrophobicity and subsequent water management issues [37,72,76]. Chun et al. [42] tested GDLs aged via an ex-situ acid-immersion test to facilitate carbon corrosion. They reported decreases in charge transfer and ionomer resistance, accompanied by an increase in the mass transport resistance peak, due to water accumulation in the GDLs. The **ORR charge transfer resistance peak (P2)** increases and shifts to lower frequencies. This increase in charge transfer resistance is most likely driven by a loss of TPB due to carbon corrosion and a reduction in CCL thickness, as well as by a loss of active catalyst particles. The peak frequency (P2) at 0.48 A cm^{-2} decreases from 65 Hz (5 000 HPCs) to 44 Hz (40 000 HPCs), while the associated capacitive contribution decreases from 13.5 mF cm^{-2} to 5.2 mF cm^{-2}. The evolution of the capacitances calculated using Eq. (7) is shown in Fig. 5, and the corresponding trend of the characteristic charge transfer frequency f_{ct} is provided in Fig. S8. A comparable decrease in frequency was also observed during high-potential cycling (1.0–1.5 V) for various CCL I/C weight ratios (0.5/0.85/1.2) [20,21]. Kwon et al. [37] reported an increase in specific relaxation time of the charge transfer (τ_o) at 0.3 A cm^{-2}

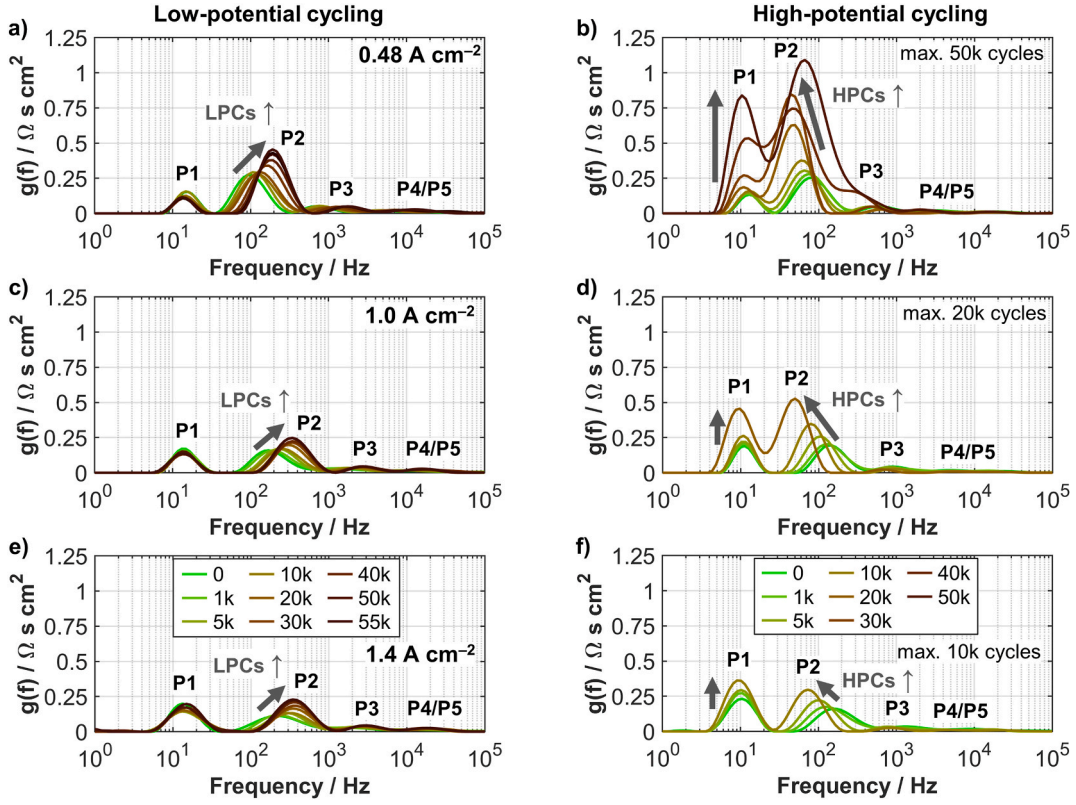

Fig. 3. Distribution of relaxation times (DRT) at 0.48, 1.0, and 1.4 A cm^{-2} (H_2/air, T = 80 °C, RH = 70% sym., $p_{O2,dry}$ = 0.315 atm, $\dot{V}$ = 200 sccm) during (a, c, e) 55 000 low-potential cycles (LPCs) and (b, d, f) 10 000–50 000 high-potential cycles (HPCs).

from 0.0076 s (132 Hz) to 0.0134 s (74 Hz) after 5 h of high-potential holding testing (1.4 V). They attributed this trend to a rapid increase in charge transfer resistance resulting from deformation of the carbon support structure and the formation of oxygen functional groups, coupled with water management issues.

In summary, the DRT shows that low-potential cycling first reduces mass transport losses, likely due to changes in water management. Later, kinetic degradation dominates, and the charge transfer peak shifts to higher frequencies. In contrast, high-potential cycling results in a delayed yet apparent increase in both mass transport and charge transfer resistance, with the peak shifting to lower frequencies. These changes align with water management issues, TPB loss, and CCL structural changes.

3.4. ORR charge transfer resistance and roughness factor

Fig. 4 clearly shows that the ORR charge transfer resistance, determined by ECM fitting to the EIS under H_2/air conditions, decreases with increasing current density, as expected for Butler-Volmer-type behavior [24]. Focusing first on **low-potential cycling** (Fig. 4a), the charge transfer resistance remains nearly constant up to 10 000 LPCs. After this point, it steadily increases by 29% (0.48 A cm^{-2}), 31% (1.0 A cm^{-2}), and 56% (1.4 A cm^{-2}) until 55 000 LPCs. This evolution correlates well with the increase in the charge transfer resistance peak (P2) in the DRT (Fig. 3a, c, e). Meanwhile, the RF decreases sharply by 40% up to 10 000 LPCs. This drop may be due to the finely dispersed catalyst particles at the BoL, which result in initially high performance but also accelerate particle agglomeration and initial degradation [77,78]. It has been reported that small catalyst particle sizes lead to a large surface area but lower stability [78]. The steady charge transfer resistance and the significant decrease in RF within the first 10 000 LPCs suggest that the finely dispersed catalyst particles result in a surplus of catalyst surface area at the BoL, which is not fully utilized during the faradaic reaction. Therefore, the substantial initial decrease in RF can be observed in the CVs, but it does not affect the charge transfer resistance. After 10 000 LPCs, the decrease in RF flattens, which is likely driven by advanced particle degradation in the form of an increase in the average catalyst particle size and the dissolution of the initially finely dispersed catalyst particles.

In contrast, during **high-potential cycling** (Fig. 4b), the ORR charge transfer resistance remains nearly constant across all current densities until 10 000 HPCs, while the RF decreases significantly. According to Topalov et al. [79], the dissolution of platinum can almost entirely be suppressed by increasing the lower potential limit to 1.05 V. Nevertheless, high-potential cycling can reportedly lead to significant platinum particle growth [67] due to the loss in carbon volume, decreasing the distance between Pt particles [71]. After 10 000 cycles, the charge transfer resistance increases by 366% at 0.48 A cm^{-2} until 50 000 HPCs, while the RF decreases only moderately. This evolution is in good agreement with the substantial decrease in cell voltage (Fig. 2b) and the increase in the charge transfer resistance peak (P2) in the DRT (Fig. 3b, d, f). The simultaneous substantial increase in mass transport resistance (Fig. 7b) and only moderate decrease in RF suggest significant microstructural changes in the CCL and/or a collapse of the carbon support structure, leading to thinning of the CCL [69].

Considering both cycling conditions, the RF follows a similar pattern during LPCs (Fig. 4a) and HPCs (Fig. 4b), characterized by an initial sharp drop, followed by a slower degradation rate. This behavior has been reported in the literature for both low- and high-potential cycling [16,19]. It likely results from finely dispersed catalyst particles that initially dissolve or agglomerate quickly before stabilizing. Quantitative analysis of catalyst particle size or evolution is beyond the scope of this study. In addition, the sharp initial RF decrease does not necessarily translate into an immediate loss of the effectively utilized ORR active area under in-operando conditions, because RF is determined from H_2/N_2 at high humidity, whereas R_{ct} is extracted under H_2/air at lower humidity during faradaic operation. Pt surface located in micro- and mesopores can contribute to the CV signal via water-mediated protonic connectivity, while being only weakly utilized for ORR under the in-operando conditions.

In conclusion, these results indicate that the ORR charge transfer resistance (determined in-operando) remained nearly constant during the first 10 000 low- and high-potential cycles but increased significantly thereafter. In contrast, the RF (determined ex-operando) exhibits a pronounced initial decrease followed by a more moderate decline.

3.5. Charge transfer process capacitance and double-layer capacitance

In Fig. 5, the evolution of the double-layer capacitance determined (ex-operando) by CV (Fig. 1c and d), as well as the progression of the charge transfer process capacitance obtained (in-operando) by EIS (H_2/air), ECM fitting, and calculated according to Eq. (7), are shown as a function of LPCs (Fig. 5a) and HPCs (Fig. 5b).

The double-layer capacitance determined by CV primarily reflects

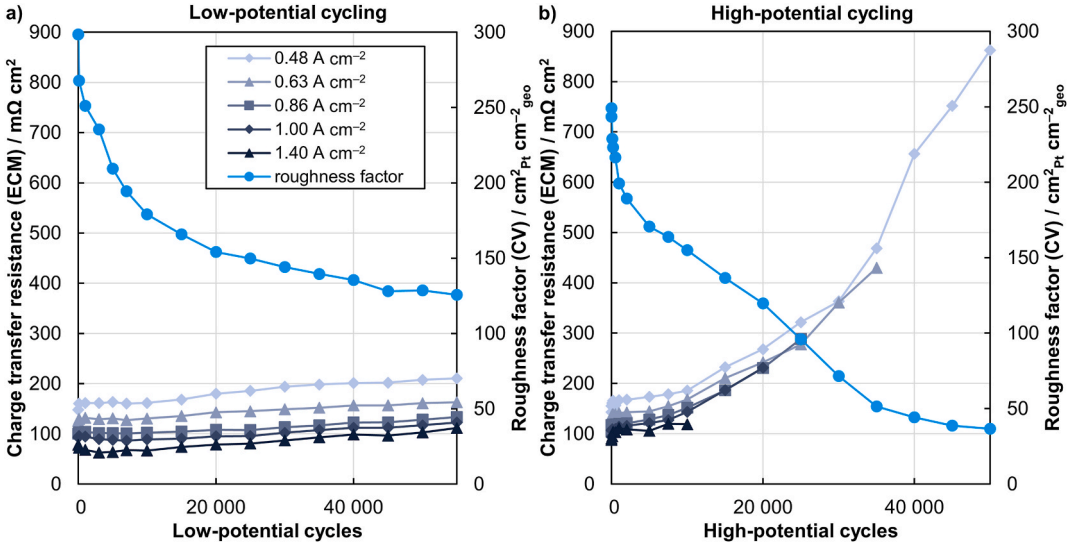

Fig. 4. Cathode roughness factor (H_2/N_2, 150 mV s^{-1}, T = 50 °C, RH = 95%, $\dot{V}$ = 200 sccm) and charge transfer resistance from ECM fitting at 0.48–1.4 A cm^{-2} (H_2/air, T = 80 °C, RH = 70% sym., $p_{O2,dry}$ = 0.315 atm, $\dot{V}$ = 200 sccm) as a function of (a) low-potential cycles (LPCs) and (b) high-potential cycles (HPCs).

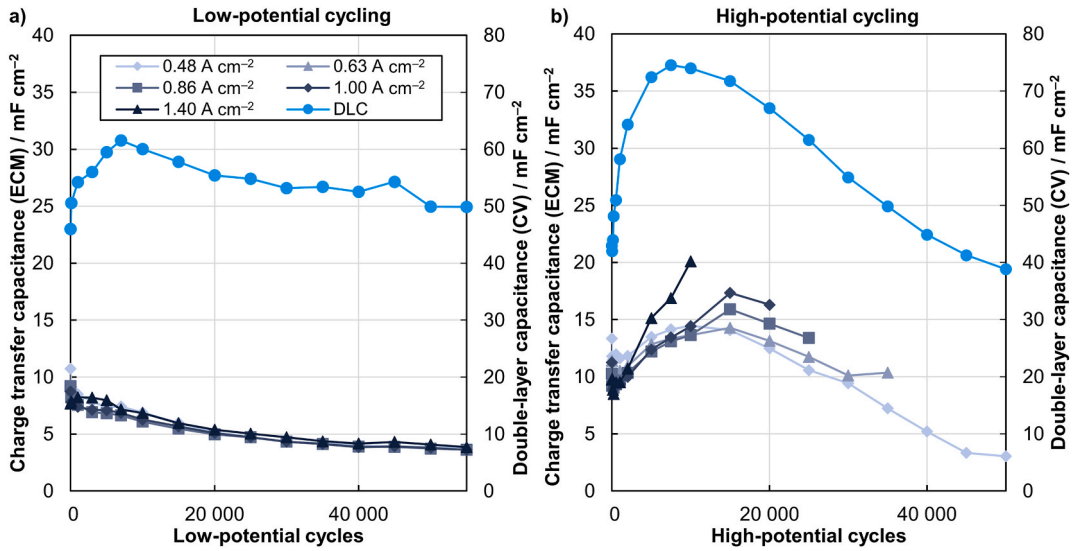

Fig. 5. Charge transfer process capacitance determined from ECM fitting at 0.48–1.4 A cm^{-2} (H_2/air, T = 80 °C, RH = 70% sym., $p_{O2,dry}$ = 0.315 atm, $\dot{V}$ = 200 sccm) and double-layer capacitance obtained by CV (H_2/N_2, T = 50 °C, RH = 95%, $\dot{V}$ = 200 sccm) as a function of (a) low-potential cycles (LPCs) and (b) high-potential cycles (HPCs).

the capacitance at the carbon and platinum interfaces, as well as oxides on the carbon surface [80]. In contrast, capacitance from the charge transfer process, determined by ECM fitting, accounts for DLC, pseudo-capacitance, and bulk capacitance, thereby capturing both interfacial and bulk processes [81]. As a result, the measured capacitances differ between techniques. Although their absolute values vary, the qualitative trends from CV and EIS agree well, validating the observed evolution. Differences in the applied methods, as well as in temperature and RH, can explain the discrepancy. CV was performed at 50 °C and 95% RH to ensure complete hydration and to achieve more clearly defined voltammogram peaks, whereas EIS was measured at 80 °C and 70% RH to reflect typical PEMFC operating conditions and to suppress flooding at high current densities. Lower RH during EIS reduces proton conductivity in the ionomer, thereby lowering capacitance [82]. In contrast, higher RH during CV helps maintain ionomer hydration, promoting better proton conductivity and resulting in higher capacitance.

During 55 000 **low-potential cycles** (Fig. 5a), the capacitances from CV and EIS decrease with the number of cycles. This decrease is driven by a loss of active catalyst sites, which reduces the available surface area for hydrogen adsorption and desorption [80]. Hu et al. [83] separated the various DLC contributions during low-potential cycling and reported a significant decrease in capacitance attributed to the carbon/water and Pt/water interface. They suggested a reduction in the accessible platinum inside the carbon support, either due to a collapse of the internal carbon structure or a decrease in the hydrophobicity of the carbon pores. While they reported a relatively constant Pt/ionomer interface contribution, they hypothesized that the increase in carbon/ionomer interface capacitance resulted from a widening of pores and/or the migration of ionomer into the carbon mesopores. Consistent with Hu et al. [83], the observed capacitance (CV and EIS) decay supports a mechanism of reduced accessible Pt as well as altered carbon porosity and hydrophobicity, aligning with our broader degradation analysis.

During the first 7 500–15 000 **high-potential cycles** (Fig. 5b), the capacitances from both methods increase sharply, then decrease until the end of life. This evolution can be attributed to two competing mechanisms [69]. The dominant mechanism in the **first phase, up to 7 500–15 000 HPCs,** is the accumulation of hydrophilic carbon corrosion products with oxygen functionalities at the carbon support surface [69,80,81,84] or the cracking of the carbon, increasing the effective carbon surface [85]. The simultaneous decrease in catalyst surface area, as indicated by the RF (Fig. 4b), suggests that the increase in capacitance (EIS) is primarily attributable to an increase in carbon surface area. In the **second phase, after 7 500–15 000 HPCs**, carbon support corrosion becomes the dominant mechanism, leading to a loss of effective carbon and platinum surfaces [69,86]. The decrease in capacitance (CV and EIS) during HPCs corresponds well with the assumed collapse of the carbon support structure after 10 000 cycles, further exacerbating the decline in DLC as the remaining active sites become less accessible, resulting in a reduced overall capacitance.

Considering the differences in operating conditions, the obtained capacitance values ranging from 38.8 to 74.5 mF cm^{-2} (CV, 50 °C, 95% RH) and 3.0 to 20.1 mF cm^{-2} (EIS, 80 °C, 70% RH) are in good agreement with capacitance values from the literature [81,85–89].

3.6. Ionomer resistance in CCL determined by EIS (H_2/air) and EIS (H_2/N_2)

Fig. 6 shows the evolution of the CCL ionomer resistance (R_{ion}), determined from ECM fitting of EIS under H_2/air conditions (in-operando) at various current densities and under H_2/N_2 conditions (ex-operando), as a function of LPCs (Fig. 6a) and HPCs (Fig. 6b). Nyquist plots of the high-frequency region of the spectra for both conditions during low- and high-potential cycling are shown in Fig. S6 and Fig. S9, respectively.

The ionomer resistance in the CCL from ex-operando EIS (H_2/N_2) follows the same qualitative trends as that from in-operando EIS (H_2/air), but is consistently higher. Although both measurements are conducted at 80 °C and 70% RH, the additional product water during H_2/air operation enhances ionomer hydration and lowers R_{ion} [90,91].

During 55 000 **low-potential cycles** (Fig. 6a), the ionomer resistance remains nearly constant at 24–31 mΩ cm^2 (H_2/air) and 35–37 mΩ cm^2 (H_2/N_2) until 10 000 LPCs, indicating a certain resilience of the ionomer structure during the initial LPCs. However, between 10 000 LPCs and 25 000–30 000 LPCs, the ionomer resistance increases significantly, suggesting a gradual ionomer degradation, structural changes in the CCL, or possibly additional degradation due to Co leaching [92,93]. After 25 000–30 000 LPCs, the ionomer resistance reaches a plateau at 35–37 mΩ cm^2 (H_2/air) and 47–49 mΩ cm^2 (H_2/N_2), respectively. Notably, the ionomer resistance changes uniformly for all current densities, indicating that the evolution in ionomer resistance is primarily driven by structural or chemical degradation of

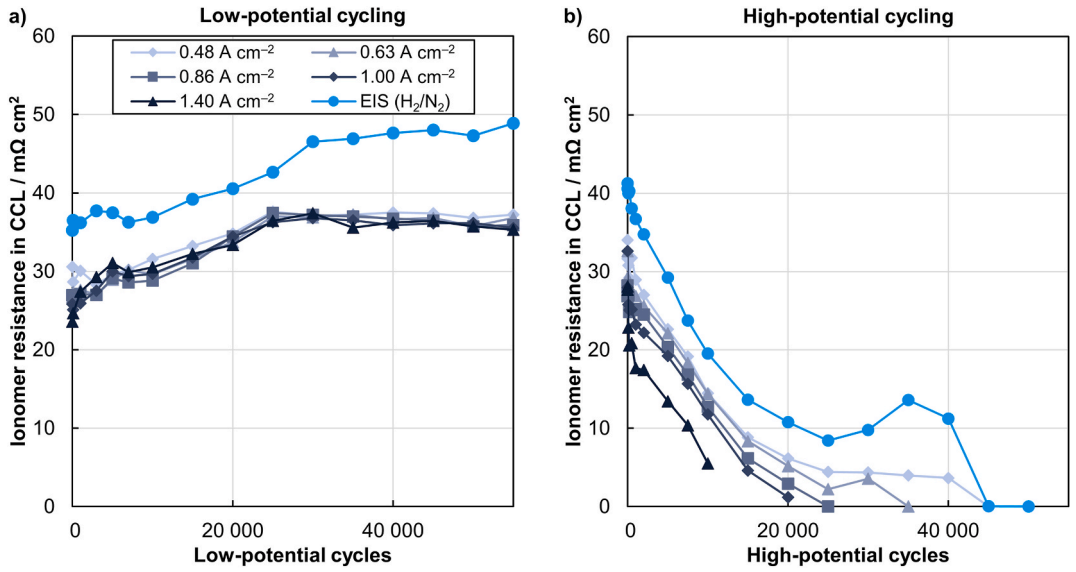

Fig. 6. Ionomer resistance of the cathode catalyst layer (CCL) determined from in-operando EIS at 0.48–1.4 A cm^{-2} (H_2/air, T = 80 °C, RH = 70% sym., $p_{O2,dry}$ = 0.315 atm, $\dot{V}$ = 200 sccm) and ex-operando EIS (H_2/N_2, T = 80 °C, RH = 70%, $\dot{V}$ = 200 sccm) as a function of (a) low-potential cycles (LPCs) and (b) high-potential cycles (HPCs).

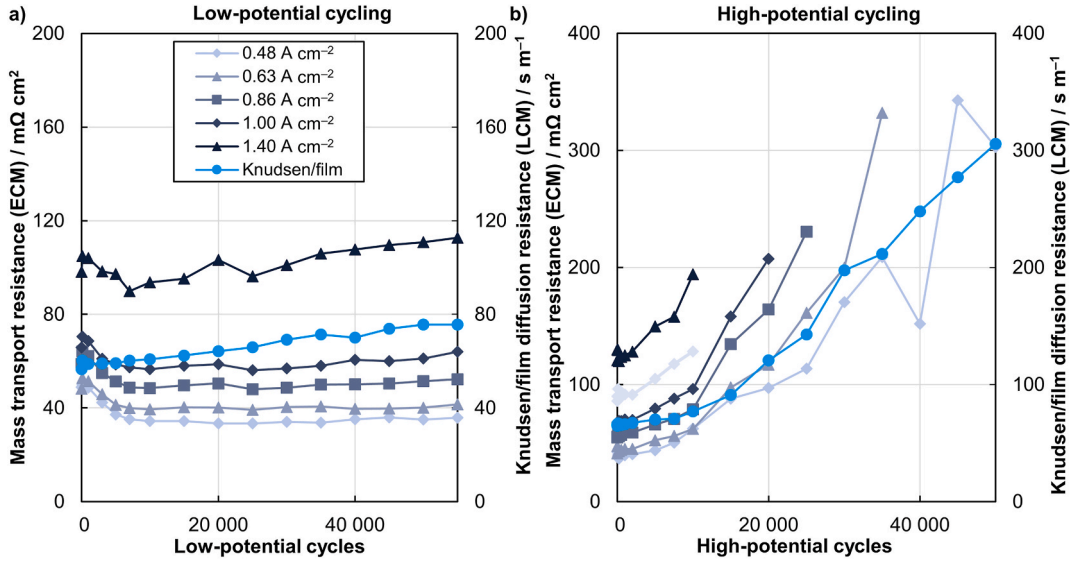

Fig. 7. Mass transport resistance determined by ECM fitting at 0.48–1.4 A cm^{-2} (H_2/air, T = 80 °C, RH = 70% sym., $p_{O2,dry}$ = 0.315 atm, $\dot{V}$ = 200 sccm) and combined Knudsen/film diffusion resistance determined by limiting current measurements (LCM, T = 80 °C, RH = 70% sym., $\dot{V}$ = 200 sccm) as a function of (a) low-potential cycles (LPCs) and (b) high-potential cycles (HPCs).

the ionomer, rather than by changes in the proton-conducting network or water management, which can vary with current density. In the literature, the reported evolution in ionomer resistance during low-potential cycling has been ambiguous. Some publications have reported no significant change in the ionomer resistance of the CCL [15–17,19], while others have reported a decrease [12,41], attributing it to a faster ionic response [37] or to electrode thinning [92]. Other studies have observed an increase due to inhomogeneities of the resistances within the CCL [94] or due to Co contamination of the cathode ionomer [92,93].

In contrast, during 50 000 **high-potential cycles** (Fig. 6b), the ionomer resistance declines steadily. This evolution likely reflects progressive structural changes in the CCL due to advanced carbon corrosion, leading to reduced CCL thickness and compaction [70], and shorter ionic pathways [19,86]. It has also been reported that high-potential cycling increases the tortuosity of ionic pathways due to changes in ionomer and water distribution within the CCL [95], which, in principle, counteract this trend. The observed decrease in ionomer resistance, therefore, suggests that the thickness reduction dominates over any opposing tortuosity effects under the present conditions. Furthermore, microstructural changes, such as the widening of carbon pores, can improve connectivity by mobilizing and redistributing the ionomer [96,97]. In the literature, the reported changes in ionomer characteristics of the CCL during high-potential cycling (1.0–1.5 V) have been ambiguous. While some have reported a monotonic increase in CCL ionomer conductivity attributed to a CCL thinning resulting in a shortening of ionic pathways [19], others have found a decrease in ionic conductivity due to higher proton transport path tortuosity as a result of changes in ionomer discontinuity and water distribution in the catalyst layers [95]. Saha et al. [86] observed an initial decrease in CCL resistance attributed to

CCL thinning, followed by an increase due to drastic changes in the ionomer network and pore structure. Chun et al. [42] reported a decrease in ionomer resistance after pre-aging of GDLs via acid-immersion tests, attributing it to improved wetting of the ionomer and membrane due to water accumulation. The current density dependence of R_{ion} and R_0 can serve as an indicator of local humidification. R_{ion} decreases with current density due to increased water production, while R_0 remains largely current independent. The corresponding trends during low- and high-potential cycling are shown in Fig. S10.

Across all tests, the ionomer resistance of the CCL was obtained from EIS (H_2/air) using the same equivalent circuit model for all current densities. The small scatter and occasional intersections between curves are within the fitting uncertainty and mainly reflect the limited sensitivity of the ECM to the ionomer resistance rather than measurement noise. As the ionomer resistance decreases,accurate fitting becomes increasingly challenging. The lowest values are therefore likely fitting artefacts rather than meaningful physical changes and should be interpreted with caution.

3.7. Mass transport resistances determined by EIS/ECM and limiting current measurements

Mass transport resistances were quantified by two complementary approaches: (i) EIS (H_2/air) combined with DRT analysis and ECM fitting, yielding the low-frequency mass transport resistance (R_{mt}^{ECM}), and (ii) limiting current measurements (LCM), providing the molecular oxygen diffusion resistance (R_{mol}^{LCM}) and the combined Knudsen/film diffusion resistance ($R_{Kn/film}^{LCM}$). In the ECM, R_{mt}^{ECM} corresponds to the oxygen transport across the GDL, MPL and inactive regions of the CCL before reaching the TPB. The molecular diffusion resistance (R_{mol}^{LCM}) arises mainly from oxygen diffusion through the gas channel, GDL, MPL and, to a lesser extent, the macropores of the CCL. In contrast, $R_{Kn/film}^{LCM}$ captures transport limitations within the micropores of the MPL and CCL (Knudsen diffusion), as well as through the thin ionomer and water films surrounding the active sites in the CCL.

Fig. 7 illustrates the evolution of the mass transport resistances (R_{mt}^{ECM}, left axis, mΩ cm^2), determined by ECM fitting for various current densities, and the combined Knudsen and film diffusion resistance ($R_{Kn/film}^{LCM}$, right axis, s m^{-1}), derived from limiting current measurements, as a function of LPCs (Fig. 7a) and HPCs (Fig. 7b). Although R_{mt}^{ECM} and $R_{Kn/film}^{LCM}$ use different units and are not combined directly, both quantify the oxygen mass transport resistance in the CCL. In Fig. 7, we therefore compare their evolution, and the consistent trends from ECM and limiting current measurements corroborate the identified changes in mass transport resistance. The molecular diffusion resistance (R_{mol}^{LCM}) of oxygen with nitrogen or helium as the inert gas did not show significant changes attributable to degradation (Fig. S11), indicating negligible structural degradation of the GDL during both AST protocols.

In Fig. 7a, the mass transport resistance (R_{mt}^{ECM}) during **low-potential cycling** initially decreases slightly during the first 10 000 LPCs, aligning with the initial decrease of the mass transport resistance peak (P1) in the DRT (Fig. 3a, c, e). In the same range, neither the combined Knudsen and film diffusion resistance (Fig. 7a) nor the molecular diffusion resistance (Fig. S11a) shows a significant decrease, indicating that the liquid water formed by the fuel cell reaction is evacuated more efficiently with progressing LPCs. This inferred change in the water management is supported by the observed reduction in polarization curve hysteresis (Fig. S3a). An initial decrease in mass transport resistance during the catalyst ASTs was also observed by others [98].

Between 10 000 and 55 000 LPCs (Fig. 7a), the mass transport resistance (R_{mt}^{ECM}) increases with a rate of 0.03 mΩ cm^2 (0.48 A cm^{-2}), 0.17 mΩ cm^2 (1.0 A cm^{-2}), and 0.42 mΩ cm^2 (1.4 A cm^{-2}) per 1 000 LPCs, while the Knudsen and film diffusion resistance ($R_{Kn/Film}^{LCM}$) increases with a rate of 0.33 s m^{-1} per 1 000 LPCs. Since the molecular diffusion resistance (R_{mol}^{LCM}) remains essentially unchanged, this behavior indicates that the additional mass transport losses originate predominantly from changes in the MPL and CCL, including the ionomer and water films, rather than from degradation of the GDL substrate. During low-potential cycling, the amount of electrochemically active catalyst decreases significantly (Fig. 4a), leading to an increase in pressure-independent mass transport resistance, particularly a rise in the specific resistance of the platinum catalyst surface [13,99].

In Fig. 7b, the mass transport resistance (R_{mt}^{ECM}) during **high-potential cycling** remains nearly constant up to 2 000 HPCs (1.4 A cm^{-2}) and 7 500 HPCs (0.48 A cm^{-2}), indicating no significant changes in water management or the CCL carbon structure. Afterward, R_{mt}^{ECM} increases significantly at all current densities with a rate of 8.23–8.25 mΩ cm^2 per 1 000 HPCs. The overlap of various processes in the frequency range becomes more pronounced as carbon corrosion progresses (see Fig. 3b), thereby affecting the separation of processes and, consequently, the fitting results. This led to the observed fitting inaccuracies of R_{mt}^{ECM}, shown in Fig. 7b, at 0.48 A cm^{-2} between 30 000–40 000 HPCs. The Knudsen and film diffusion resistance ($R_{Kn/Film}^{LCM}$), shown in Fig. 7b, increases slightly from 64.8 to 70.7 s m^{-1} until 7 500 HPCs. Afterward, $R_{Kn/Film}^{LCM}$ increases with a rate of 5.5 s m^{-1} per 1 000 cycles, which coincides with the substantial increase in R_{mt}^{ECM}. This trend can therefore be attributed to significant changes in the MPL, CCL structure, or the characteristics of the CCL ionomer film. This evolution is in good agreement with the literature, where the increase in mass transport resistance during carbon structure ASTs has been attributed to a collapse of the carbon support structure [67–69] and a decrease in CCL porosity [67]. Furthermore, a decrease in hydrophobicity of the CCL surface [76] and GDL degradation [100–102] can impede oxygen transport by accumulating liquid water within the pores of the CCL and GDL.

3.8. Distribution of the electrochemical resistances during ASTs

In Fig. 8, the distribution of all resistances (ohmic, charge transfer, CCL ionomer, and mass transport) determined by ECM fitting is shown at the beginning and end of life for low-potential cycling (a, c) and high-potential cycling (b, d) at 0.48 A cm^{-2} and 1.4 A cm^{-2}.

During **low-potential cycling**, the total resistance (R_{total}) increases by 20% (0.48 A cm^{-2}) and 27% (1.4 A cm^{-2}). At the BoL, the total resistance (0.48 A cm^{-2}) consists of the ORR charge transfer (60%), mass transport (20%), CCL ionomer (12%), and ohmic resistance (8%). At 1.4 A cm^{-2}, the contribution of the mass transport resistance makes up 45%, while the charge transfer resistance only accounts for 36% of the total resistance. After 55 000 LPCs, the total resistance at 0.48 A cm^{-2} is dominated by the ORR charge transfer resistance (69%), while at 1.4 A cm^{-2} it is approximately equally shared between the ORR charge transfer and mass transport resistances (40%). Overall, these results indicate that low-potential cycling primarily increases catalyst-related charge transfer losses while leaving mass transport pathways essentially unchanged. As a result, the total resistance is more strongly governed by kinetics, especially at moderate current density.

During **high-potential cycling,** the total resistance increases by 384% (0.48 A cm^{-2}) and 35% (1.4 A cm^{-2}) with significant changes in the individual contributions. After high-potential cycling, the total resistance at 0.48 A cm^{-2} is composed of charge transfer resistance (72%), mass transport resistance (25%), and ohmic resistance (3%). In contrast, at 1.4 A cm^{-2}, mass transport resistance dominates at both the BoL (46%) and after 10 000 HPCs (56%). Therefore, high-potential cycling leads to significant deterioration of the cathode catalyst layer, thereby greatly amplifying charge transfer and mass transport losses. Consequently, the total resistance is even more dominated by charge transfer at low current density and by mass transport limitations at high current density.

To relate these resistance changes to structural modifications in the

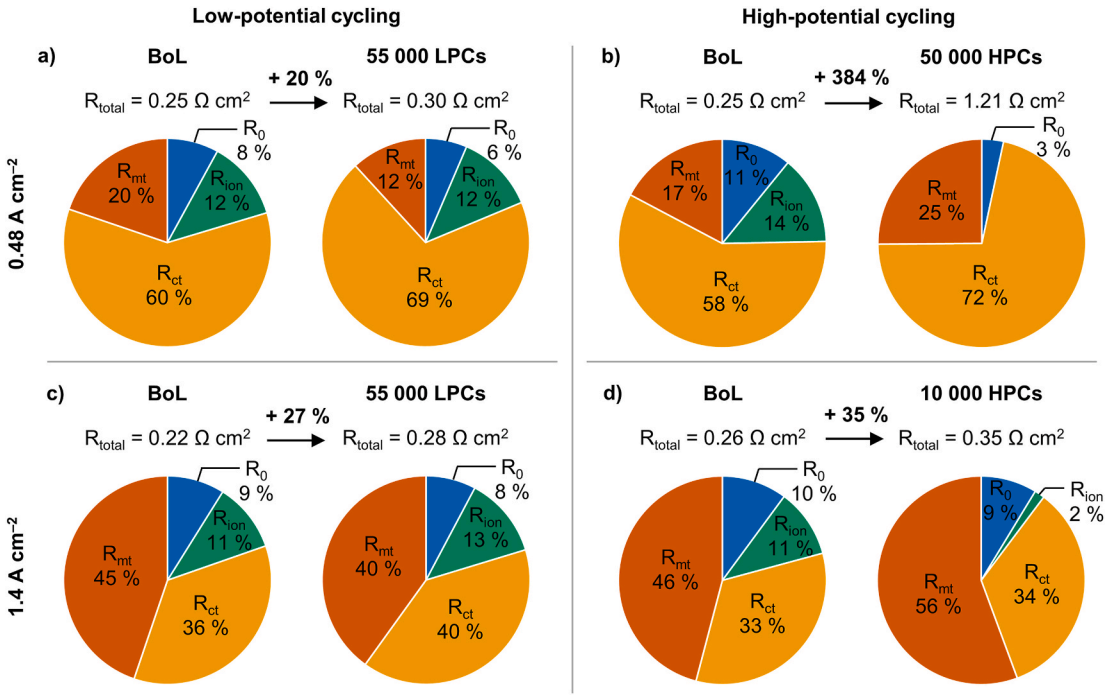

Fig. 8. Distribution of all resistances determined from ECM fitting (H_2/air, T = 80 °C, RH = 70% sym., $p_{O2,dry}$ = 0.315 atm, $\dot{V}$ = 200 sccm) at 0.48 and 1.4 A cm^{-2} during (a, c) low-potential cycling and (b, d) high-potential cycling.

MEA, **cross-sectional analysis** of the MEAs before and after the ASTs (Fig. S12 and Table S8) was performed. Notably, no significant changes in the membrane, anode catalyst layer, or CCL thickness were detected during low-potential cycling. In contrast, at high-potential cycling, the CCL thickness decreased significantly from 15.8 µm to 3.7 µm, corresponding to a 77% reduction (about 1.5% per 1 000 HPCs), while the membrane and anode catalyst layer thickness were unaffected. The combination of a 77% reduction in CCL thickness and the substantial increase in charge transfer and mass transport resistance during HPCs indicates that the CCL compaction not only reduces the available TPB area but also lengthens and/or narrows the effective oxygen transport pathways. Under these conditions, even small residual inhomogeneities in water distribution or local hydrophobicity can lead to pronounced transport bottlenecks, consistent with the sharp rise in Knudsen and film diffusion resistance. Although the present analysis does not resolve local through-plane or in-plane non-uniformities, the trends in thickness and resistance strongly support a scenario of severe carbon support collapse and loss of accessible porosity in the CCL/MPL. Direct visualization of the pore structure (e.g., via FIB-SEM or X-ray tomography) is beyond the scope of this study, but our findings are consistent with microstructural observations reported in Refs. [22,67,70] under similar high-potential cycling conditions.

4. Conclusion

This study provides a detailed analysis of the effects of accelerated stress tests (DOE protocols) comprising 55 000 low-potential cycles and 50 000 high-potential cycles on the degradation of PEMFC cathode catalyst layers. We used in-operando H_2/air electrochemical impedance spectroscopy, distribution of relaxation times, transmission line modeling, limiting current measurements, and complementary ex-operando diagnostics to separate and quantify the evolution of ohmic, charge transfer, CCL ionomer, and mass transport losses during catalyst- and carbon support structure degradation.

In the case of **low-potential cycling** (0.6–0.95 V), the charge transfer resistance remained stable for up to 10 000 cycles, while the ohmic, CCL ionomer, and mass transport resistances changed only modestly. After 10 000 cycles, the charge transfer resistance increased by about 1.1 mΩ cm^2 per 1 000 cycles at 0.48 A cm^{-2}, accounting for most of the performance loss by the end of life. Increases in ohmic and mass transport resistance remained comparatively small. Therefore, low-potential cycling mainly increased kinetic losses associated with catalyst degradation, while electronic and transport pathways within the CCL and gas diffusion media remained largely unaffected.

High-potential cycling (1.0–1.5 V) showed a qualitatively different, two-phase behavior. An initial quasi-steady regime up to about 7 500–10 000 cycles was followed by a rapid deterioration in which charge transfer and mass transport resistances rose synchronously by about 16.9 and 6.0 mΩ cm^2 per 1 000 cycles (at 0.48 A cm^{-2}), respectively. Limiting current measurements showed a pronounced increase in Knudsen and film diffusion resistance, indicating that oxygen transport in the CCL and MPL became the dominant limitation. At the end of life, a 77% reduction in CCL thickness coincided with a measurable increase in ohmic resistance of about 0.3 mΩ cm^2 per 1 000 cycles. This behavior indicates severe degradation of contact resistance and electronic pathways, a collapse of the carbon support structure, and a significant decrease in TPB area.

These results align with previous studies showing that high-potential and SU/SD conditions primarily cause carbon corrosion, catalyst layer collapse, and transport issues, whereas low-potential cycling primarily accelerates catalyst degradation with a minor impact on transport properties. Building on this, the present study extends prior EIS and DRT research by applying both low- and high-potential cycling protocols (DOE) to otherwise identical cells and by quantifying loss contributions as a function of cycle number and current density. Furthermore, the findings underscore the impact of operational factors on CCL properties and the need for realistic in-operando testing conditions to properly assess PEMFC degradation. The use of EIS, distribution of relaxation times, transmission line modeling, and complementary in- and ex-operando diagnostic methods provides a comprehensive picture of the degradation within the cathode catalyst layer.

Beyond the mechanistic insights, the EIS, DRT, and TLM framework provides practical value for engineering tasks. By separating ohmic, charge transfer, CCL ionomer, and mass transport resistance, along with

their characteristic frequencies, from a single in-operando EIS dataset, this approach enables rapid screening of advanced carbon supports and low-PGM cathode catalyst layers with respect to their dominant loss modes. In addition, the approach increases AST diagnostic efficiency by distinguishing kinetic, ionic, and transport limitations without requiring multiple complementary measurements at each aging step. Finally, because EIS can be implemented intermittently during operation, the extracted resistances and frequencies provide suitable observables for state-of-health monitoring and early warning of shifts in the prevailing degradation mechanism. These use cases are particularly relevant for catalyst layer concepts with strongly modified local oxygen transport, such as HOPI-based systems.

CRediT authorship contribution statement

Sebastian Raab: Writing – review & editing, Writing – original draft, Validation, Project administration, Methodology, Investigation, Formal analysis, Data curation, Conceptualization. **André Weber:** Writing – review & editing, Supervision, Resources, Funding acquisition.

Declaration of generative AI and AI-assisted technologies in the manuscript preparation process

During the preparation of this work, the authors used ChatGPT 5.2 in order to assist with grammar and language review during the drafting of this manuscript. After using this tool, the authors reviewed and edited the content as needed and take full responsibility for the content of the published article.

Declaration of competing interest

The authors declare that they have no known competing financial interests or personal relationships that could have appeared to influence the work reported in this paper.

Acknowledgements

The authors would like to thank Dr.-Ing. Tobias Goosmann for carefully proofreading the manuscript and for his valuable comments.

Appendix A. Supplementary data

Supplementary data to this article can be found online at https://doi.org/10.1016/j.jpowsour.2026.239725.

Data availability

The data presented in this study are available in the KITopen repository under https://doi.org/10.35097/7401chq88xc0h8a2.

References

[1] D.A. Cullen, K.C. Neyerlin, R.K. Ahluwalia, R. Mukundan, K.L. More, R.L. Borup, A.Z. Weber, D.J. Myers, A. Kusoglu, Nat. Energy 6 (2021) 462–474, https://doi.org/10.1038/s41560-021-00775-z.
[2] R.L. Borup, A. Kusoglu, K.C. Neyerlin, R. Mukundan, R.K. Ahluwalia, D.A. Cullen, K.L. More, A.Z. Weber, D.J. Myers, Curr. Opin. Electrochem. 21 (2020) 192–200, https://doi.org/10.1016/j.coelec.2020.02.007.
[3] P. Urchaga, T. Kadyk, S.G. Rinaldo, A.O. Pistono, J. Hu, W. Lee, C. Richards, M. H. Eikerling, C.A. Rice, Electrochim. Acta 176 (2015) 1500–1510, https://doi.org/10.1016/j.electacta.2015.03.152.
[4] B.D. James, J.H. Huya-Kouadio, C. Houchins, D.A. DeSantis. Strategic Analysis, Inc, Arlington, VA, USA, 2017. https://doi.org/10.13140/RG.2.2.36532.55683.
[5] M.M. Whiston, I.L. Azevedo, S. Litster, K.S. Whitefoot, C. Samaras, J.F. Whitacre, Proc. Natl. Acad. Sci. U. S. A. 116 (2019) 4899–4904, https://doi.org/10.1073/pnas.1804221116.
[6] P.J. Ferreira, G.J. la O', Y. Shao-Horn, D. Morgan, R. Makharia, S. Kocha, H. A. Gasteiger, J. Electrochem. Soc. 152 (2005) A2256–A2271, https://doi.org/10.1149/1.2050347.
[7] R.K. Ahluwalia, S. Arisetty, J.-K. Peng, R. Subbaraman, X. Wang, N. Kariuki, D. J. Myers, R. Mukundan, R. Borup, O. Polevaya, J. Electrochem. Soc. 161 (2014) F291–F304, https://doi.org/10.1149/2.051403jes.
[8] G.P. Keeley, S. Cherevko, K.J. Mayrhofer, ChemElectroChem 3 (2016) 51–54, https://doi.org/10.1002/celc.201500425.
[9] D.J.S. Sandbeck, M. Inaba, J. Quinson, J. Bucher, A. Zana, M. Arenz, S. Cherevko, ACS Appl. Mater. Interfaces 12 (2020) 25718–25727, https://doi.org/10.1021/acsami.0c02801.
[10] S. Stariha, N. Macauley, B.T. Sneed, D. Langlois, K.L. More, R. Mukundan, R. L. Borup, J. Electrochem. Soc. 165 (2018) F492–F501, https://doi.org/10.1149/2.0881807jes.
[11] U. S. Department of Energy, The Fuel Cell Technologies Office Multi-Year Research, Development, and Demonstration Plan, 2016. Washington, DC.
[12] P. Schneider, A.-C. Scherzer, L. Ney, H.-K. Kwon, B.D. Storey, D. Gerteisen, N. Zamel, Sci. Data 11 (2024) 828, https://doi.org/10.1038/s41597-024-03662-w.
[13] G.S. Harzer, J.N. Schwämmlein, A.M. Damjanović, S. Ghosh, H.A. Gasteiger, J. Electrochem. Soc. 165 (2018) F3118–F3131, https://doi.org/10.1149/2.0161806jes.
[14] P. Schneider, A.-C. Scherzer, B.D. Storey, M. Klingele, N. Zamel, D. Gerteisen, J. Electrochem. Soc. 170 (2023) 104505, https://doi.org/10.1149/1945-7111/acff1f.
[15] T. Lazaridis, R.K.F. Della Bella, H.A. Gasteiger, J. Electrochem. Soc. 171 (2024) 064506, https://doi.org/10.1149/1945-7111/ad5624.
[16] R.K.F. Della Bella, B.M. Stühmeier, H.A. Gasteiger, J. Electrochem. Soc. 169 (2022) 044528, https://doi.org/10.1149/1945-7111/ac67b8.
[17] L.I. Astudillo, H.A. Gasteiger, J. Electrochem. Soc. 170 (2023) 124512, https://doi.org/10.1149/1945-7111/ad10e9.
[18] S. Komini Babu, D. Spernjak, J. Dillet, A. Lamibrac, G. Maranzana, S. Didierjean, O. Lottin, R.L. Borup, R. Mukundan, Appl. Energy 254 (2019) 113659, https://doi.org/10.1016/j.apenergy.2019.113659.
[19] A. Perego, A. Avid, D.N. Mamania, Y. Chen, P. Atanassov, H. Yildirim, M. Odgaard, I.V. Zenyuk, Appl. Catal. B Environ. 301 (2022) 120810, https://doi.org/10.1016/j.apcatb.2021.120810.
[20] S. Raab, A. Karmakar, P.-Y.A. Chuang, A. Weber, J. Electrochem. Soc. 172 (2025) 114508, https://doi.org/10.1149/1945-7111/ae1b3d.
[21] S. Raab, P.-Y.A. Chuang, A. Weber, ECS Trans. 114 (2024) 351–366, https://doi.org/10.1149/11405.0351ecst.
[22] S. Ghosh, H. Ohashi, H. Tabata, Y. Hashimasa, T. Yamaguchi, J. Power Sources 362 (2017) 291–298, https://doi.org/10.1016/j.jpowsour.2017.07.017.
[23] T. Tamaki, H. Wang, N. Oka, I. Honma, S.-H. Yoon, T. Yamaguchi, Int. J. Hydrogen Energy 43 (2018) 6406–6412, https://doi.org/10.1016/j.ijhydene.2018.01.205.
[24] M. Heinzmann, A. Weber, E. Ivers-Tiffée, J. Power Sources 402 (2018) 24–33, https://doi.org/10.1016/j.jpowsour.2018.09.004.
[25] M. Heinzmann, A. Weber, E. Ivers-Tiffée, J. Power Sources 444 (2019) 227279, https://doi.org/10.1016/j.jpowsour.2019.227279.
[26] H. Yuan, H. Dai, P. Ming, X. Wang, X. Wei, Appl. Energy 303 (2021) 117640, https://doi.org/10.1016/j.apenergy.2021.117640.
[27] G. Avioz Cohen, D. Gelman, Y. Tsur, J. Phys. Chem. C 125 (2021) 11867–11874, https://doi.org/10.1021/acs.jpcc.1c03667.
[28] T. Reshetenko, A. Kulikovsky, Electrochim. Acta 391 (2021) 138954, https://doi.org/10.1016/j.electacta.2021.138954.
[29] Y. Shen, C. Chang, J. Fu, X. Sun, Chem. Eng. J. 510 (2025) 161561, https://doi.org/10.1016/j.cej.2025.161561.
[30] X. Zhang, L. Huang, Y. Jiang, L. Lin, H. Liao, W. Liu, Appl. Energy 355 (2024) 122286, https://doi.org/10.1016/j.apenergy.2023.122286.
[31] D. Zhu, Y. Yang, T. Ma, Sustainability 14 (2022) 5677, https://doi.org/10.3390/su14095677.
[32] X. Zhang, Y. Jiang, L. Huang, W. Chen, D. Brett, Electrochim. Acta 391 (2021) 138925, https://doi.org/10.1016/j.electacta.2021.138925.
[33] Y. Ao, Z. Li, S. Laghrouche, D. Depernet, D. Candusso, K. Zhao, J. Power Sources 603 (2024) 234420, https://doi.org/10.1016/j.jpowsour.2024.234420.
[34] S.S. Araya, F. Zhou, S.L. Sahlin, S. Thomas, C. Jeppesen, S.K. Kær, Energies 12 (2019) 152, https://doi.org/10.3390/en12010152.
[35] M.A. Travassos, V.V. Lopes, R.A. Silva, A.Q. Novais, C.M. Rangel, Int. J. Hydrogen Energy 38 (2013) 7684–7696, https://doi.org/10.1016/j.ijhydene.2013.01.132.
[36] J. Zuo, N.Y. Steiner, Z. Li, D. Hissel, Appl. Energy 378 (2025) 124762, https://doi.org/10.1016/j.apenergy.2024.124762.
[37] J. Kwon, P. Choi, S. Jo, H. Oh, K.-Y. Cho, Y.-K. Lee, S. Kim, K. Eom, Electrochim. Acta 414 (2022) 140219, https://doi.org/10.1016/j.electacta.2022.140219.
[38] Z. Liu, M. Yang, X. Tang, L. Shi, S. Xu, Q. Zhou, Appl. Energy 401 (2025) 126647, https://doi.org/10.1016/j.apenergy.2025.126647.
[39] Z. Hu, L. Xu, Q. Gan, X. Du, W. Dai, Q. Wang, W. Zheng, Y. Ding, J. Li, M. Ouyang, Electrochim. Acta 389 (2021) 138627, https://doi.org/10.1016/j.electacta.2021.138627.
[40] Z. Gu, T. Ma, J. Chen, J. Appl. Electrochem. 54 (2024) 2241–2253, https://doi.org/10.1007/s10800-024-02095-y.
[41] D. Yoo, S. Park, S. Oh, M.P. Kim, K. Park, Materials 17 (2024) 4425, https://doi.org/10.3390/ma17174425.
[42] H. Chun, J.H. Chang, J.-w. Kim, J. Sim, K. Min, Int. J. Hydrogen Energy 71 (2024) 831–844, https://doi.org/10.1016/j.ijhydene.2024.05.154.
[43] J.D. Fairweather, B. Li, R. Mukundan, J. Fenton, R.L. Borup, ECS Trans. 33 (2010) 433–446, https://doi.org/10.1149/1.3484542.
[44] E. Colombo, A. Bisello, A. Casalegno, A. Baricci, J. Electrochem. Soc. 168 (2021) 054508, https://doi.org/10.1149/1945-7111/abf4eb.

[45] G. Hinds, E. Brightman, Electrochem. Commun. 17 (2012) 26–29, https://doi.org/10.1016/j.elecom.2012.01.007.
[46] M. Heinzmann, A. Weber, J. Power Sources 558 (2023) 232540, https://doi.org/10.1016/j.jpowsour.2022.232540.
[47] K.G. Co, Freudenberg Performance Materials GmbH, Freudenberg Gas Diffusion Layers – Fuel Cell – Technical Data, Freudenberg Performance Materials GmbH & Co. KG, Weinheim, Germany, 2025.
[48] S. Kabir, D.J. Myers, N. Kariuki, J. Park, G. Wang, A. Baker, N. Macauley, R. Mukundan, K.L. More, K.C. Neyerlin, ACS Appl. Mater. Interfaces 11 (2019) 45016–45030, https://doi.org/10.1021/acsami.9b11365.
[49] G. Tsotridis, A. Pilenga, G. De Marco, T. Malkow, Joint Research Centre (JRC), European Commission, 2015, https://doi.org/10.2790/54653.
[50] A.J. Bard, L.R. Faulkner, Electrochemical Methods: Fundamentals and Applications, second ed., Wiley & Sons, 2001.
[51] D.M. Morales, M. Risch, J. Phys. Energy 3 (2021) 034013, https://doi.org/10.1088/2515-7655/abee33.
[52] T.V. Reshetenko, J. St-Pierre, J. Electrochem. Soc. 161 (2014) F1089–F1100, https://doi.org/10.1149/2.1021410jes.
[53] J. St-Pierre, Fuel Cells 11 (2011) 263–273, https://doi.org/10.1002/fuce.201000092.
[54] M. Schönleber, D. Klotz, E. Ivers-Tiffée, Electrochim. Acta 131 (2014) 20–27, https://doi.org/10.1016/j.electacta.2014.01.034.
[55] N. Wagner, K.A. Friedrich, Fuel Cells 9 (2009) 237–246, https://doi.org/10.1002/fuce.200800071.
[56] M. Boillot, C. Bonnet, N. Jatroudakis, P. Carre, S. Didierjean, F. Lapicque, Fuel Cells 6 (2006) 31–37, https://doi.org/10.1002/fuce.200500101.
[57] V. Brichzin, J. Fleig, H. Habermeier, G. Cristiani, J. Maier, Solid State Ionics 152–153 (2002) 499–507, https://doi.org/10.1016/S0167-2738(02)00379-X.
[58] J. Bisquert, Phys. Chem. Chem. Phys. 2 (2000) 4185–4192, https://doi.org/10.1039/b001708f.
[59] M. Ahadi, M. Tam, J. Stumper, M. Bahrami, Int. J. Hydrogen Energy 44 (2019) 3603–3614, https://doi.org/10.1016/j.ijhydene.2018.12.016.
[60] J. Zhao, H. Liu, X. Li, Electrochem. Energy Rev. 6 (2023) 13, https://doi.org/10.1007/s41918-022-00175-1.
[61] D. Klotz, J.P. Schmidt, A. Kromp, A. Weber, E. Ivers-Tiffée, ECS Trans. 41 (2012) 25–33, https://doi.org/10.1149/1.3692958.
[62] D. Malevich, B.R. Jayasankar, E. Halliop, J.G. Pharoah, B.A. Peppley, K. Karan, J. Electrochem. Soc. 159 (2012) F888–F895, https://doi.org/10.1149/2.007301jes.
[63] K.C. Neyerlin, W. Gu, J. Jorne, A. Clark, H.A. Gasteiger, J. Electrochem. Soc. 154 (2007) B279–B287, https://doi.org/10.1149/1.2400626.
[64] B. Hirschorn, M.E. Orazem, B. Tribollet, V. Vivier, I. Frateur, M. Musiani, Electrochim. Acta 55 (2010) 6218–6227, https://doi.org/10.1016/j.electacta.2009.10.065.
[65] G.J. Brug, A.L.G. van den Eeden, M. Sluyters-Rehbach, J.H. Sluyters, J. Electroanal. Chem. Interfacial Electrochem. 176 (1984) 275–295, https://doi.org/10.1016/s0022-0728(84)80324-1.
[66] N.E. Souza, J.L. Bott-Neto, T.A. Rocha, G.C. da Silva, E. Teixeira-Neto, E. R. Gonzalez, E.A. Ticianelli, Electrochim. Acta 265 (2018) 523–531, https://doi.org/10.1016/j.electacta.2018.01.180.
[67] H. Schulenburg, B. Schwanitz, N. Linse, G.G. Scherer, A. Wokaun, J. Krbanjevic, R. Grothausmann, I. Manke, J. Phys. Chem. C 115 (2011) 14236–14243, https://doi.org/10.1021/jp203016u.
[68] Z.Y. Liu, B.K. Brady, R.N. Carter, B. Litteer, M. Budinski, J.K. Hyun, D.A. Muller, J. Electrochem. Soc. 155 (2008) B979–B984, https://doi.org/10.1149/1.2956198.
[69] A.P. Young, J. Stumper, E. Gyenge, J. Electrochem. Soc. 156 (2009) B913–B922, https://doi.org/10.1149/1.3139963.
[70] N. Macauley, D.D. Papadias, J. Fairweather, D. Spernjak, D. Langlois, R. Ahluwalia, K.L. More, R. Mukundan, R.L. Borup, J. Electrochem. Soc. 165 (2018) F3148–F3160, https://doi.org/10.1149/2.0061806jes.
[71] L. Strandberg, V. Shokhen, M. Skoglundh, B. Wickman, ACS Catal. 14 (2024) 8494–8504, https://doi.org/10.1021/acscatal.4c00417.
[72] X. Zhang, Y. Yang, L. Guo, H. Liu, Int. J. Hydrogen Energy 42 (2017) 4699–4705, https://doi.org/10.1016/j.ijhydene.2016.08.223.
[73] J. Zhao, X. Li, Energy Convers. Manag. 199 (2019) 112022, https://doi.org/10.1016/j.enconman.2019.112022.
[74] J.E. Owejan, P.T. Yu, R. Makharia, ECS Trans. 11 (2007) 1049–1057, https://doi.org/10.1149/1.2781018.
[75] J. Sim, M. Kang, K. Min, E. Lee, J.-Y. Jyoung, Renew. Energy 190 (2022) 959–970, https://doi.org/10.1016/j.renene.2022.04.015.
[76] J.-H. Park, S.-D. Yim, T. Kim, S.-H. Park, Y.-G. Yoon, G.-G. Park, T.-H. Yang, E.-D. Park, Electrochim. Acta 83 (2012) 294–304, https://doi.org/10.1016/j.electacta.2012.07.117.
[77] R. Makharia, S. Kocha, P. Yu, M.A. Sweikart, W. Gu, F. Wagner, H.A. Gasteiger, ECS Trans. 1 (2006) 3–18, https://doi.org/10.1149/1.2214540.
[78] Z. Yang, S. Ball, D. Condit, M. Gummalla, J. Electrochem. Soc. 158 (2011) B1439–B1445, https://doi.org/10.1149/2.081111jes.
[79] A.A. Topalov, S. Cherevko, A.R. Zeradjanin, J.C. Meier, I. Katsounaros, K.J. J. Mayrhofer, Chem. Sci. 5 (2014) 631–638, https://doi.org/10.1039/c3sc52411f.
[80] A.P. Young, V. Colbow, D. Harvey, E. Rogers, S. Wessel, J. Electrochem. Soc. 160 (2013) F381–F388, https://doi.org/10.1149/2.061304jes.
[81] R. Alink, M. Schüßler, M. Pospischil, D. Erath, D. Gerteisen, J. Power Sources 327 (2016) 526–534, https://doi.org/10.1016/j.jpowsour.2016.07.084.
[82] J.H. Jang, S. Jeon, J.H. Cho, S.-K. Kim, S.-Y. Lee, E. Cho, H.-J. Kim, J. Han, T.-H. Lim, J. Electrochem. Soc. 156 (2009) B1293–B1300, https://doi.org/10.1149/1.3187928.
[83] L. Hu, T. Van Cleve, H. Yu, J.H. Park, N. Kariuki, A.J. Kropf, R. Mukundan, D. A. Cullen, D.J. Myers, K.C. Neyerlin, J. Power Sources 556 (2023) 232490, https://doi.org/10.1016/j.jpowsour.2022.232490.
[84] H. Nara, S. Tominaka, T. Momma, T. Osaka, J. Electrochem. Soc. 158 (2011) B1184–B1191, https://doi.org/10.1149/1.3610988.
[85] F.S. Saleh, E.B. Easton, J. Electrochem. Soc. 159 (2012) B546–B553, https://doi.org/10.1149/2.098205jes.
[86] P. Saha, K. Khedekar, H. Wang, P. Atanassov, L. Cheng, S. Stewart, C. Johnston, I. V. Zenyuk, J. Mater. Chem. A 10 (2022) 12551–12562, https://doi.org/10.1039/d2ta02666j.
[87] Y. Liu, M. Murphy, D. Baker, W. Gu, C. Ji, J. Jorne, H.A. Gasteiger, ECS Trans. 11 (2007) 473–484, https://doi.org/10.1149/1.2780961.
[88] C. Gerling, M. Hanauer, U. Berner, K.A. Friedrich, J. Electrochem. Soc. 168 (2021) 084504, https://doi.org/10.1149/1945-7111/ac1812.
[89] J.P. Sabawa, A.S. Bandarenka, Results Chem. 2 (2020) 100078, https://doi.org/10.1016/j.rechem.2020.100078.
[90] Y. Liu, M.W. Murphy, D.R. Baker, W. Gu, C. Ji, J. Jorne, H.A. Gasteiger, J. Electrochem. Soc. 156 (2009) B970–B980, https://doi.org/10.1149/1.3143965.
[91] K. Shinozaki, H. Yamada, Y. Morimoto, J. Electrochem. Soc. 158 (2011) B467–B475, https://doi.org/10.1149/1.3556906.
[92] X. Wang, L. Hu, K.C. Neyerlin, R.K. Ahluwalia, J. Electrochem. Soc. 170 (2023) 024503, https://doi.org/10.1149/1945-7111/acb847.
[93] C. Lee, X. Wang, J.K. Peng, A. Katzenberg, R.K. Ahluwalia, A. Kusoglu, S. Komini Babu, J.S. Spendelow, R. Mukundan, R.L. Borup, ACS Appl. Mater. Interfaces 14 (2022) 35555–35568, https://doi.org/10.1021/acsami.2c07085.
[94] A.A. Nechitailov, P. Volovitch, N.V. Glebova, A. Krasnova, Membranes 13 (2023) 342, https://doi.org/10.3390/membranes13030342.
[95] Y. Qi, Y. Huang, Z. Gao, C.H. Chen, A. Perego, H. Yildirim, M. Odgaard, T. Asset, P. Atanassov, I.V. Zenyuk, J. Power Sources 551 (2022) 232209, https://doi.org/10.1016/j.jpowsour.2022.232209.
[96] S. Ott, A. Orfanidi, H. Schmies, B. Anke, H.N. Nong, J. Hubner, U. Gernert, M. Gliech, M. Lerch, P. Strasser, Nat. Mater. 19 (2020) 77–85, https://doi.org/10.1038/s41563-019-0487-0.
[97] L. Amichi, H. Yu, A. Ziabari, O. Rahman, D. Arregui-Mena, L. Hu, K.C. Neyerlin, D.A. Cullen, Adv. Energy Mater. 14 (2024) 2402310, https://doi.org/10.1002/aenm.202402310.
[98] Q. Meyer, Y. Zeng, C. Zhao, J. Power Sources 437 (2019) 226922, https://doi.org/10.1016/j.jpowsour.2019.226922.
[99] T.A. Greszler, D. Caulk, P. Sinha, J. Electrochem. Soc. 159 (2012) F831–F840, https://doi.org/10.1149/2.061212jes.
[100] W. Yoshimune, A. Kato, T. Hayakawa, S. Yamaguchi, S. Kato, npj Mater. Degrad. 8 (2024) 106, https://doi.org/10.1038/s41529-024-00524-z.
[101] S. Yu, X. Li, S. Liu, J. Hao, Z. Shao, B. Yi, RSC Adv. 4 (2014) 3852–3856, https://doi.org/10.1039/c3ra45770b.
[102] H. Liu, M.G. George, M. Messerschmidt, R. Zeis, D. Kramer, J. Scholta, A. Bazylak, J. Electrochem. Soc. 164 (2017) F695–F703, https://doi.org/10.1149/2.0071707jes.